Journal of Membrane Science 715 (2025) 123476

Contents lists available at ScienceDirect

Journal of Membrane Science

journal homepage: www.elsevier.com/locate/memsci

The effect of Sharklet patterns on thermal efficiency and salt-scaling resistance of poly (vinylidene fluoride) membranes during direct contact membrane distillation

Shouhong Fan [a,**], Duong T. Nguyen [b], Jaylene Martinez [a], John Chau [c], Kieran Fung [a], Kamalesh Sirkar [c], Anthony P. Straub [b], Yifu Ding [a,*]

[a] *Membrane Application, Science, and Technology (MAST) Center, Paul M. Rady Mechanical Engineering, University of Colorado at Boulder, Boulder, CO, 80309, USA*
[b] *Civil, Environmental, and Architectural Engineering, University of Colorado at Boulder, Boulder, CO, 80309, USA*
[c] *Membrane Application, Science and Technology (MAST) Center, Chemical and Materials Engineering, New Jersey Institute of Technology, Newark, NJ, 07102, USA*

ARTICLE INFO

Keywords:
Sharklet-patterned membranes
Thermally induced phase separation
Direct contact membrane distillation
Temperature polarization
Hypersaline brine treatment

ABSTRACT

Membrane distillation (MD) can treat high-salinity brine. However, the system's efficiency is hindered by obstacles, including salt scaling and temperature polarization. When properly implemented, surface patterns can improve the mass and heat transfer in the boundary layer, which leads to higher MD efficiency. In this work, the performance of direct contact membrane distillation (DCMD) using Sharklet-patterned poly (vinylidene fluoride) (PVDF) membranes is investigated. Both non-patterned and patterned PVDF membranes are prepared by lithographically templated thermally induced phase separation (*lt*-TIPS) process with optimized conditions. Sharklet patterns on the membranes improve the DCMD performance: up to 17 % higher water flux and 35 % increased brine-side heat transfer coefficient. The scaling resistance of the membranes during DCMD is tested by both saturated $CaSO_4$ solution and hypersaline NaCl solutions. Patterned PVDF membranes show an average of 30 % higher water flux and up to 45 % lessened flux decline over time compared with non-patterned membranes when treating high-concentration brines. Post-mortem analysis reveals that Sharklet-patterned membranes display less salt-scaling on surfaces with smaller-sized $CaSO_4$ and NaCl crystals, maintain a relatively cleaner surface, and exhibit better retention of hydrophobicity.

1. Introduction

With the rapid population growth and climate change, freshwater scarcity is becoming a major societal challenge [1–3]. There is an estimated 141.5 million m^3 of concentrated brine generated from desalination plants annually [4], which needs to be treated. Membrane distillation (MD) is capable of treating hypersaline brine with a total dissolved solids (TDS) of 75–300 g/L [5–9]. MD process relies on a thermal gradient to recover fresh water from high-salinity wastewater [10,11]. Specifically, water vapor from the hot brine side permeates through a hydrophobic microporous membrane and condenses on the colder distillate side [12,13]. The hydrophobicity of the membrane prevents liquid brine from penetrating the pores, allowing MD to achieve a theoretical salt rejection >99 %. These attributes render MD a promising component technology for achieving zero liquid discharge (ZLD) [14–16].

Despite the advantages, MD processes suffer from brine leakage and low water permeation due to salt scaling and temperature polarization [17–20]. The inherent mass and heat transport mechanism in the MD process results in not only concentration polarization (typical for most membrane processes) but also temperature polarization within the boundary layer near the membrane surface [21–23]. To overcome these challenges, both chemical and physical modifications of MD membranes were investigated [24]. For example, resistance against salt-scaling was improved by coating membranes with fluorinated titanium dioxide (TiO_2) nanoparticles [25], carbon nanotubes (CNTs) [26], PDMS/silica particles [27], and CF_4 plasma treatment [28]. The alleviation of temperature polarization *via* localized heating was also extensively studied by coating materials that can be resistively heated [29,30] or photothermally heated [31–33] near the membrane surface.

** Corresponding author.
* Corresponding author.
E-mail addresses: shouhong@seas.upenn.edu (S. Fan), yifu.ding@colorado.edu (Y. Ding).

https://doi.org/10.1016/j.memsci.2024.123476
Received 1 July 2024; Received in revised form 1 November 2024; Accepted 2 November 2024

On the other hand, the integrations of feed spacers and patterned membrane modules as turbulence promoters were effective at mitigating temperature polarization and scaling. For example, spacers in the shape of either cylindrical filaments or non-woven meshes improved the flux by up to 60 % and brine-side heat transfer coefficient by up to two-fold, compared to the counterparts without spacers [34,35]. Additionally, patterned membrane modules with geometries resembling the shape of spacers were shown to be capable of enhancing the flux by 28 %, reducing temperature polarization by 7 %, and promoting higher scaling resistance against gypsum salts [36].

Surface patterning shows great promise in improving the active surface area and local hydrodynamics near the membrane surface [37–43]. Recent advances in patterned membranes for MD include the impartment of micropillars, prisms, and corrugations on membrane surfaces [44–46]. In combination with superhydrophobic and omniphobic surface chemistry and operation optimizations such as pulsed flow and negative feed pressure, patterned membranes achieved promising scaling resistance and salt rejection for the MD process [44,47,48].

Sharklet patterns, which are essentially the bio-mimicking sharkskin features, are excellent at improving the hydrodynamics above the membrane surface by triggering turbulences and secondary flows under crossflow conditions [49]. Sharklet patterns were successfully imparted on PVDF membranes through a lithographically templated thermally induced phase separation (*lt*-TIPS) process [50]. The patterned membranes exhibited superior surface integrity and enhanced MD performance in terms of water flux and liquid entry pressure (LEP) compared with their non-patterned counterparts [51]. Compared with other patterning techniques, like nanoimprinting lithography (NIL) and phase inversion micromolding (PSμM), *lt*-TIPS yields patterned membranes with a narrower pore size distribution, higher surface porosity and symmetric pore structure, which are desirable for MD process [52,53]. Despite this, it remains unclear whether the Sharklet patterns, which exhibit high bio-fouling resistance [54], are effective in mitigating the salt-scaling and temperature polarization for the MD.

In this study, the impact of Sharklet patterns on the MD performance was quantified. Specifically, (1) the *lt*-TIPS technique is optimized to fabricate PVDF membranes suitable for MD study, and (2) a direct contact membrane distillation (DCMD) system is used to compare the performance of non-patterned and patterned PVDF membranes in terms of water flux, brine-side heat transfer, thermal efficiency, and salt-scaling resistance.

2. Experimental

2.1. Materials

PVDF with a molecular weight of 530,000 g/mol was purchased from Scientific Polymer Products Inc. Tributyl *O*-acetylcitrate (ATBC) was purchased from Sigma Aldrich (purity >98 %). PDMS precursor and crosslinker (Sylgard ® 184 kit) were purchased from Dow Corning, USA. Ethanol and sodium chloride (NaCl) were purchased from Fisher Chemicals. Calcium sulfate dihydrate ($CaSO_4 \cdot 2H_2O$) was also purchased from Sigma Aldrich. The DI water was sourced from a Millipore Milli-Q ® Integral 10 Water Purification System. All the chemicals and polymers were used without any additional modifications.

2.2. Membrane fabrication

Fig. 1 depicts the steps of patterning PVDF membranes *via* the *lt*-TIPS process. To maximize the DCMD water flux, thinner membranes are desirable. The *lt*-TIPS process using the sandwich-casting method generally leads to membranes with thickness >300 μm [50]. In this study, a doctor blade (blade-to-mold distance = 300 μm) was used to cast membranes with thicknesses of approximately 210 μm. A PDMS replica (precursor: crosslinker ratio = 10 : 1) of the master Sharklet film (Sharklet Technologies, USA) was fabricated using standard soft lithography [50,51].

A 25 wt% PVDF/ATBC solution was prepared by mixing at 185 °C for 1 h under nitrogen protection until the polymer solution turned clear. The 25 wt% was used because of its relatively low viscosity for blade-casting, which still yields patterned membranes with adequate mechanical strength [51]. The PVDF/ATBC solution was quickly poured onto a PDMS template and cast by a doctor blade at speeds of 0.5, 1.2, and 3.0 inch/s. The solution cast on the PDMS mold was placed in open air at 23 °C for 30 min to allow complete phase separation. Next, the nascent membrane on the PDMS mold was immersed in ethanol overnight at room temperature to promote membrane demolding and full extraction of ATBC. The membranes were freeze-dried for 2 h to prevent warping and then were sealed in Ziploc bags at room temperature for subsequent tests. Control (non-patterned) PVDF membranes were fabricated using flat PDMS mold as the templates under otherwise identical conditions. In addition to direct air cooling, 23 °C DI water was also examined as a quenching medium because of the negligible solubility of ATBC in water [55].

2.3. Membrane characterizations

Morphology of the surface and cross-section of all PVDF membranes were characterized using a field emission scanning electron microscope (FESEM JEOL JSM-7401F, Japan). The cross-sections of the membrane samples were prepared by fracturing in liquid nitrogen. To minimize the charging effect during imaging, all the samples were coated with a 5 nm layer of platinum with a sputter coater (Cressington 108 Auto).

To quantify the dimensions of the patterns replicated on the PVDF membranes, an atomic force microscope (AFM, Asylum Cypher, Bruker, USA) was applied under tapping mode using an Al-coated All-in One cantilever probe (150 kHz nominal natural frequency, Budget Sensor). The fast scan direction was kept perpendicular to the pattern ridges to trace the features accurately. The scan area was 30 μm × 30 μm for all the samples. Averaged values of the width and height of the pattern ridges from five randomly selected regions were used to determine the pattern replication fidelity [56].

The overall porosity (Ɛ) of the PVDF membranes was estimated by

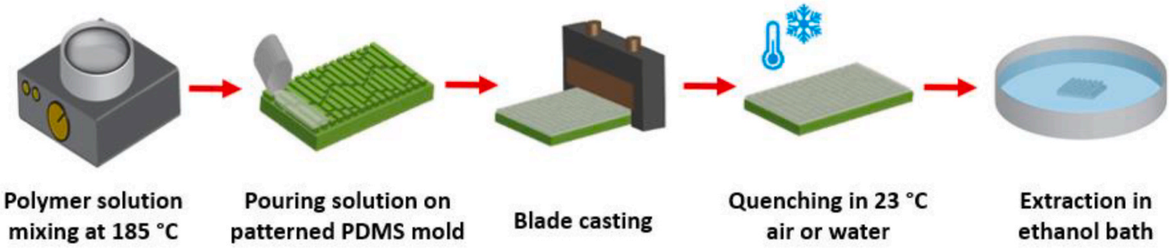

Fig. 1. Schematic illustration of the steps of replicating Sharklet patterns from PDMS template onto PVDF membranes. Non-patterned membrane fabrication is performed by replacing the patterned PDMS mold with a flat-surface mold with identical mold thickness.

gravimetric measurements [57] as

$$\varepsilon = \left(1 - \frac{\frac{m}{\rho}}{A \times l}\right) \times 100\% \tag{1}$$

where m, A, and l correspond to the mass, membrane area, and thickness of the membrane sample, while ρ is the density of bulk PVDF (=1.76 g/cm^3 as specified by the manufacturer).

The pore sizes of all the membranes were characterized by an automated lab-made gas-liquid displacement porometer [58]. A membrane sample was immersed into n-butanol for 20 min to ensure all the open pores were wetted. Subsequently, the wetting liquid was displaced by the ultra-high purity N_2 gas with a stepwise increase of pressure (0.5 psi for every 5 s). The maximum pore diameter ($d_{\max}$) was calculated from the pressure at which the N_2 started to permeate through the membrane, while the mean pore diameter (d_{mean}) was calculated from the pressure at which the N_2 flow rate approached half of the linear gas flow region (pressure vs. N_2 flow rate), respectively, by using the Young-Laplace equation

$$d = \frac{4\gamma \times \cos\theta}{\Delta P} \tag{2}$$

where ΔP is the transmembrane pressure, γ is the surface tension of n-butanol (=24.5 dyn/cm), and the contact angle (θ) equals 0° as butanol thoroughly wets the membrane pores [58]. The average pore size of each membrane is reported based on measurements of at least three samples.

The water contact angle of the membranes was determined by an optical tensiometer (Biolin Scientific) using a sessile-drop method (2 μL DI-water droplet). At least three repeated measurements were carried out for each sample, and the average values are reported here. The LEP of the membranes was measured at room temperature by a dead-end DI water permeation setup with a 2.0 psi/min stepwise pressure increase. The LEP value is taken as the pressure at which a water drop is first observed on the permeate side of the membrane. The average values of five repeated measurements for each membrane are reported.

2.4. DCMD study

The DCMD tests were performed using a bench-scale system, as illustrated in Fig. S1. For all the tests, the Sharklet pattern ridges were aligned perpendicularly to the brine flow direction, which was shown to display the most enhanced hydrodynamics [41].

For the brine-side heat transfer coefficient measurement, the feed was a 10 g/L NaCl aqueous solution. Such a relatively low salt concentration was chosen to ensure that the water vapor pressure was not significantly impacted by the dissolved salt but still allowed monitoring of the potential membrane wetting (through ionic conductivity measurements) during the DCMD test [59,60]. The brine and distillate were kept at 60 °C and 20 °C, respectively. The circulating flow rate of the distillate was maintained at 0.25 L/min. In contrast, the flow rate of the feed varied between 0.24, 0.43, and 0.66 L/min to systematically assess the dependence of brine-side heat transfer on the brine flow rate. Correspondingly, the average brine flow velocity was 0.07, 0.13, and 0.20 m/s, respectively, estimated using the cross-sectional area of 5.52×10^{-5} m^2 for the feed channel. Note that 0.66 L/min was picked as the maximum flow rate, which was determined experimentally as brine leakages occurred above 0.70 L/min, indicating the liquid pressure of brine surpasses the LEP of membranes. A membrane module made of acrylic plastic was used to minimize the heat lost to the surroundings [61]. Due to the limited size of the Sharklet replica mold, the surface area of the membrane sample was maintained at ~5.5 cm^2 (~2.9 cm in length and ~1.9 cm in width) for all the DCMD tests.

The DCMD of hypersaline brine was performed with two types of salt solutions, $CaSO_4$ and NaCl. A saturated $CaSO_4$ solution (2.0 g/L) and two NaCl solutions with initial concentrations of 189 g/L and 314 g/L were chosen to accelerate the scaling during DCMD [62]. Throughout all the tests, the temperatures of brine and distillate were maintained at 60 °C and 20 °C, while the brine and distillate flow rates were kept at 0.65 and 0.25 L/min, respectively. It is worth mentioning that a higher brine flow rate was purposely chosen for two reasons: (1). to obtain the highest measurable water flux during hypersaline DCMD because of the detrimental effect of high salt concentration on the water flux [59]; (2). to enable higher hydraulic pressure on the brine side of the membrane for quick scaling detection [63]. The DCMD of the saturated $CaSO_4$ solution continued until a brine leakage was observed. The DCMD of the 189 g/L NaCl solution continued until the brine concentration reached 331 g/L (terminated at 72 h for the protection of the gear pump). Then, to assess the scaling resistance of patterned membranes against saturated NaCl solution, the initial NaCl concentration was further increased to 314 g/L. The DCMD test for this NaCl solution ran continuously for about 40 h until NaCl started to precipitate from the brine reservoir, indicating the feed brine reached ~370 g/L (the solubility limit of NaCl at 60 °C). For these DCMD tests, the brine solutions circulated in a closed loop circle between the membrane module and a feed reservoir of 500 mL or 1000 mL holding $CaSO_4$ and NaCl, respectively (Fig. S1). A bigger feed reservoir was used for NaCl because of the longer scaling time.

For all DCMD tests, the water flux was calculated by measuring the mass change of the distillate, while the salt rejection (R) was calculated as

$$R = \left(1 - \frac{C_P}{C_f}\right) \times 100\% = \left[1 - \frac{C_P}{\left(\frac{V_n \times c_b}{V_d + V_n}\right) \times a}\right] \times 100\% \tag{3}$$

where C_P is the electrical conductivity of the bulk permeate measured at 20 °C. C_f is the electrical conductivity of permeate, assuming all brine permeates through the membrane with salt rejection of 0 %. C_f can be estimated through the linear correlation between the conductivity and salt concentration of the permeate. Specifically, V_n is the volume of permeate collected at a given amount of time, V_d is the initial volume of the distillate, and c_b is the concentration of salt in the feed brine. Additionally, a is a constant derived from the linear correlation between the salt concentration and electrical conductivity (shown in Fig. S2). For all the patterned membranes, the Sharklet-patterned side (active side) was in direct contact with the feed, while the non-pattern side (flipped side) was mounted towards the distillate side.

3. Result and discussion

3.1. Characterizations of membranes fabricated using lt-TIPS

The *lt*-TIPS process was first optimized to fabricate suitable membranes for the DCMD study. From the prior work [50], the *lt*-TIPS process using the sandwich-casting method resulted in membranes thicker than 300 μm. To fabricate thinner membranes appropriate for the MD process, a blade-casting method was used in the *lt*-TIPS process. Specifically, the thickness of all PVDF membranes was controlled at 210 ± 10 μm. Note the Sharklet patterns have a negligible effect on the membrane thickness, considering the height of replicated patterns is only 2.2 μm at maximum. Fig. 2 reveals the surface morphology of non-patterned and patterned membranes prepared by air quenching (Fig. 2a and b) and water quenching (Fig. 2c and d) with a casting speed of 3.0 inch/s. For the non-patterned membranes, blade-casting yielded much smaller (~2 μm) surface defects than the sandwich-casting method (~10–20 μm) [50]. Sharklet patterns were successfully replicated on the membranes prepared by both air- and water-quenching, and no surface defects were observed on the patterned membranes.

Different quenching media and casting speeds did not lead to any noticeable difference in pattern replication quality and surface integrity (Fig. S3 – Fig. S5). However, the membranes formed by water-quenching

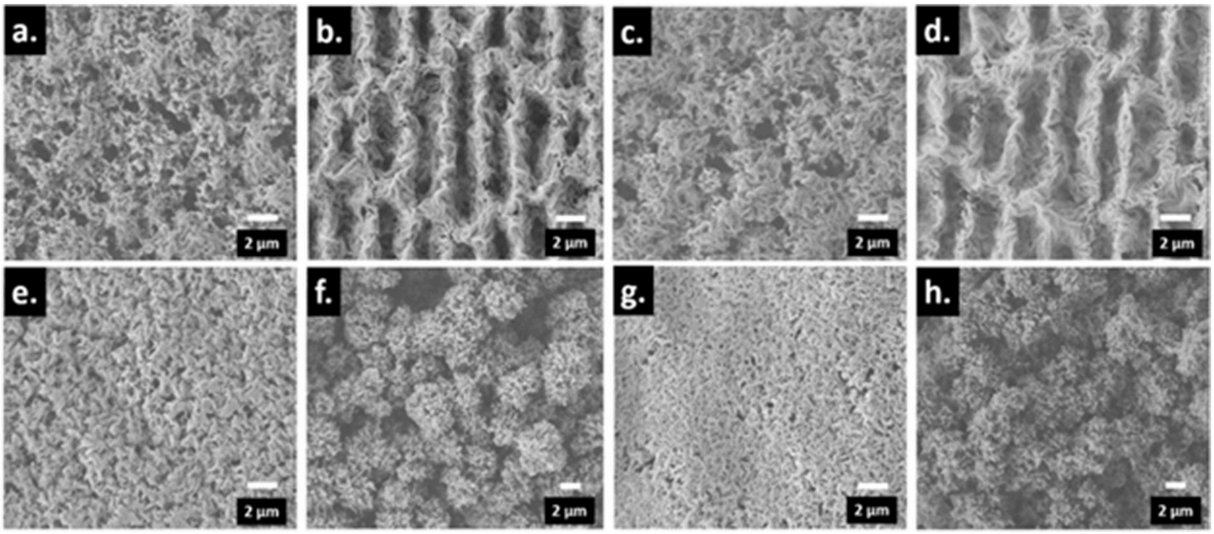

Fig. 2. SEM images of PVDF membranes prepared using different quenching media. (a) Top surface of the air-quenched non-patterned membrane, (b) top surface of the air-quenched patterned membrane, (c) top surface of the water-quenched non-patterned membrane, (d) top surface of the water-quenched patterned membrane, (e) bottom surface and (f) cross-section of the air-quenched patterned membrane, (g) bottom surface and (h) cross-section of the water quenched patterned membrane. All the membranes were prepared at a casting speed of 3.0 inch/s.

showed fewer open pores with smaller pore sizes on the top surface (Fig. 2b *vs*. 2d), the "flipped side" surface (Fig. 2e *vs*. 2g), and the cross sections (Fig. 2f *vs*. 2h). Such a trend, similarly observed in membranes fabricated using PVDF/dibutyl phthalate (DBP) and poly(4-methyl-1-pentene) (PMP)/cyclohexane systems, is attributed to the faster quenching rate in water than in air [64,65]. The more rapid PVDF solidification in water leads to less domain coarsening and, thus, smaller and fewer pore openings [66–68]. Lastly, all the membranes displayed spherulitic morphology because the PVDF/ATBC concentration is above the monotectic point (24 %), and the solution goes through a solid-liquid (S-L) phase separation [69]. The size of the spherulites appears to be slightly smaller and more densely packed for water-quenched membranes than air-quenched ones at all casting speeds (Fig. 2f and h and Fig. S6), again, due to the faster quenching kinetics in water. Note that spherulitic morphology is not conducive to improving the mechanical strength of the PVDF membranes due to the loosely connected polymer domains. The tensile strength and fracture strain of *lt*-TIPS patterned PVDF membranes having identical polymer concentrations are typically less than 2 MPa and 10 %, respectively [50,51]. The co-solvent approach is recommended to induce liquid-liquid (L-L) phase separation to form membranes with cellular morphology, which has higher mechanical strength.

There was no discernible difference in the morphology between the "flipped side" and the cross-section between the patterned and non-

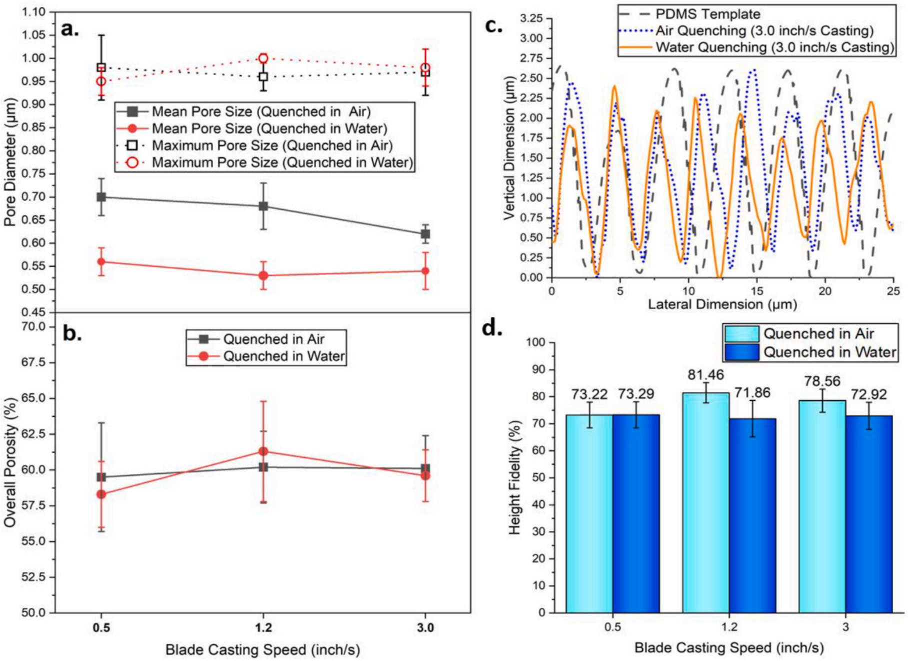

Fig. 3. (a) Maximum and mean pore diameter, and (b) overall porosity of patterned membranes prepared by different casting speeds and quenching media. (c) AFM topographical profiles of Sharklet patterns on PDMS mold (dashed), replicated on PVDF membranes prepared by air-quenching (dotted) and water-quenching (solid); (d) height fidelity of Sharklet pattern replication on membranes using different quenching media and casting speeds.

patterned membranes prepared under identical conditions. The pore size and overall porosity of the patterned membranes are summarized in Fig. 3a and b, respectively. Data for non-patterned membranes are shown in Fig. S7. The $d_{\max}$ of non-patterned and patterned membranes were independent of the quenching medium and casting speed (Fig. 3a and Fig. S7a). Interestingly, the $d_{\max}$ of patterned membranes (0.95 μm–1.0 μm) was slightly smaller than that of the non-patterned membranes (1.1 μm–1.3 μm) according to the pore size distribution (Fig. S8). The smaller $d_{\max}$ of patterned membranes could be attributed to the patterns-enhanced surface integrity, which was reported in the prior works on *lt*-TIPS [50,51]. Specifically, the trenches of Sharklet patterns could act as the physical barriers that constrain the coarsening of diluents into large domains as it would on flat surfaces during phase separation, thus eliminating defect formation on the patterned surfaces (Fig. 2a and b). In contrast, the d_m of non-patterned membranes did not significantly differ from that of the patterned PVDF membranes prepared by the same condition (~6 % difference, within the error range) (Fig. 3a and Fig. S7a). Rather, it was dictated by the quenching medium as manifested by the d_m of air-quenched membranes being 15 %–25 % larger than that of the water-quenched ones. This difference in d_m is in accordance with the above-discussed morphology difference between the air- and water-quenched membranes, and it is consistent with the trend observed for PVDF/DBP and PMP/cyclohexane systems [64,65].

Regardless of the casting speed and quenching medium, the overall porosity of the membranes (Fig. 3b and Fig. S7b) was ~60 %. Generally, the solvents are extracted from nascent membranes after TIPS to create the interconnected pores within the membrane matrix. Thus, it is assumed that the initial dope composition or the solvent content determines the final membrane porosity [67]. The discrepancy between 60 % membrane porosity and 75 % solvent concentration is attributed to the membrane shrinkage during solvent extraction and drying. Note that higher porosity is desirable for MD application, and further process development, e.g., using co-solvent to induce the intrinsically more porous bi-continuous cellular structure, is preferable to improve the membrane porosity, therefore, the membrane's permeability.

The patterning fidelity is the ratio between the average height (or width) of the replicated patterns and the depth (or width) of the cavities of the PDMS mold, which can be quantified by the AFM (Fig. 3c). As summarized in Fig. 3d, higher height fidelity was observed for air-quenched membranes than water-quenched membranes, at casting speeds of 1.2 inch/s and 3.0 inch/s. The width fidelity was 74 %–76 %, regardless of the casting speed and quenching medium (Fig. S9). Compared with the sandwich-casting method (53 % for height fidelity and 61 % for width fidelity [50]), the blade-casting method yielded higher patterning fidelity. The improvements could be attributed to the better cavity filling of the PDMS mold by the PVDF/ATBC solution driven by the shear stress exerted by the casting blade. Note that the 80 % patterning fidelity is the highest value achieved by a single solvent *lt*-TIPS system, as well as one of the highest among all the reported membrane-patterning techniques [52,56].

The LEP is the minimum hydrostatic pressure at which liquid penetrates membrane pores [70,71]. The LEP of patterned (19.0 psi – 20.5 psi) and non-patterned (16.5 psi – 17.6 psi) membranes showed negligible dependence on casting speed and quenching medium, contributing to less than 1.0 psi difference among membranes with the same surface morphology (Fig. 4a and b). LEP is typically dictated by the $d_{\max}$ of the membrane (Fig. 3a and Fig. S7a) [72]. Evidently, the higher surface integrity of patterned membranes (smaller $d_{\max}$) leads to a higher LEP, which is beneficial for DCMD.

Based on all the characterizations discussed above, air-quenching with a casting speed of 3.0 inch/s was used to fabricate all the membranes for the following DCMD studies. The fabricated non-patterned and patterned membranes showed WCA of 116.4 ± 1.6° and 137.5± 1.8°, respectively. The increase in WCA on patterned membranes, desirable for MD applications, is caused by the composite-wetting effect from pattern-enhanced surface roughness [73].

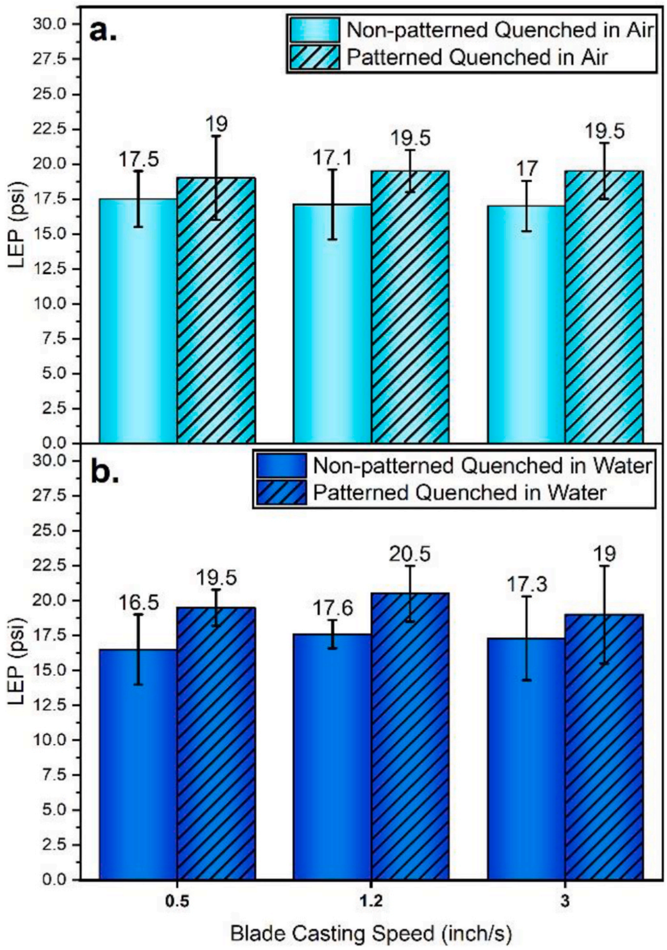

Fig. 4. LEP of patterned and non-patterned membranes prepared using different casting speeds and quenching media: (a) air-quenching and (b) water-quenching.

3.2. DCMD brine-side heat transfer analysis

In DCMD, convective heat transfer from the brine provides the energy for continuous water evaporation at the brine/air interface near the membrane surface [74]. The total transmembrane heat transfer rate (Q_t) of the DCMD system can be expressed as

$$Q_t = q_t A_m \tag{4}$$

where q_t is the total heat flux and A_m is the effective surface area of the membrane.

Assuming no heat is lost to the ambient surroundings, once the flat-sheet membrane DCMD system reaches a steady state with constant water flux, the convective heat transfer rate and heat flux of brine and distillate are equal to that of the total DCMD system as

$$Q_t = Q_b = Q_d \tag{5}$$

$$q_t = q_b = q_d \tag{6}$$

where Q_b (q_b) and $Q_d(q_d)$ are the heat transfer rates (heat flux) at the brine side and the distillate side of DCMD, respectively. Q_b and Q_d can be calculated by the total heat transfer from the brine into the distillate according to the following equations

$$Q_b = \rho_b C_{pb} F_{bi} T_{bi} - \rho_b C_{pb} F_{bo} T_{bo} \tag{7}$$

$$Q_d = \rho_w C_{pw} F_{do} T_{do} - \rho_w C_{pw} F_{di} T_{di} \tag{8}$$

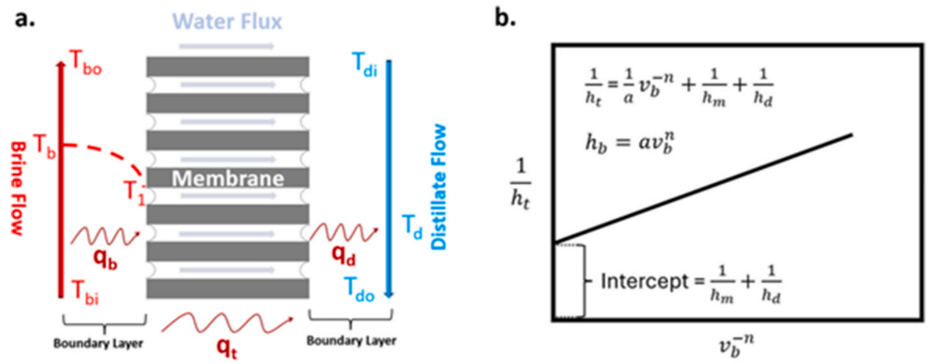

Fig. 5. (a) Schematic illustration of the heat transfer and temperature polarization on the brine side in a DCMD system; (b) Correlation between the brine flow velocity and total heat transfer resistance based on the Wilson-plot method (replotted according to Ref. [60]).

where ρ_b (ρ_w) and $C_{pb}\left(C_{pw}\right)$ are the density and heat capacity of brine (water), respectively. T_{bi} (T_{di}) and T_{bo} (T_{do}) are the measured brine (distillate) temperatures at the flow channel inlet and outlet of the DCMD module, respectively. The brine (distillate) flow rate at the inlet F_{bi} (F_{di}) and outlet F_{bo} (F_{do}) can be estimated as

$$F_{do} - F_{di} = F_{bi} - F_{bo} = F_p \tag{9}$$

where F_p is the collected water vapor permeate flow rate [60].

The temperature profiles and heat transfer in the DCMD system are schematically illustrated in Fig. 5a. At the steady state, temperature polarization occurs in a boundary layer where the brine-side effective membrane temperature (T_1) is lower than the bulk feed temperature (T_b) [22,60]. Temperature polarization reduces the actual driving force for water permeation and, consequently, the efficiency of DCMD. Despite its significance, T_1 is challenging to measure directly because of the potential disturbance to the fluid flow. Instead, a Wilson-plot method is often employed to determine T_1 [60], as described below. In this regard, Q_b and Q_t can be expressed as

$$Q_b = q_b A_m = h_b(T_b - T_1)A_m \tag{10}$$

$$Q_t = q_t A_m = h_t(T_b - T_d)A_m \tag{11}$$

where h_b and h_t are the brine-side and total heat transfer coefficient, respectively. T_d is the temperature of the bulk distillate.

The total heat transfer resistance (reciprocal of the total heat transfer coefficient) can be expressed as the sum of resistances from each component of the DCMD membrane module for an in-series model

$$\frac{1}{h_t} = \frac{1}{h_b} + \frac{1}{h_m} + \frac{1}{h_d} \tag{12}$$

where h_m and h_d are the membrane and distillate heat transfer coefficients, correspondingly. By treating the feed brine as fully developed flow, h_b can be expressed as [60,75]

$$h_b = av_b^n \tag{13}$$

where a is a constant, v_b is the brine flow velocity and n is the corresponding velocity exponent. By combing equations (12) and (13), the total heat transfer resistance of DCMD can be expressed as a linear function of v_b^{-n}.

$$\frac{1}{h_t} = \frac{1}{a}v_b^{-n} + \frac{1}{h_m} + \frac{1}{h_d} \tag{14}$$

To account for the potential effect of heat loss to the ambient surroundings during water evaporation on the hot brine side, h_t at each corresponding brine flow speed was calculated based on the heat transfer rate on the distillate side by combining equations (8) and (11). The data obtained (Figs. S10a and S10b) were fitted first with a proper n to achieve a linear correlation between v_b^{-n} and $\frac{1}{h_t}$. Then, $\frac{1}{h_b}$ could be determined based on the slope of the Wilson plot and the intercept $\frac{1}{h_m}+\frac{1}{h_d}$ (Fig. 5b). The linearly-fitted Wilson plots and associated equations are summarized in Figs. S10c and S10d. Specifically, the values of n for the non-patterned and patterned membranes are 0.62 and 0.58, respectively. The value of n for non-patterned PVDF membranes in different cells was 0.6 [60]. The power law dependence of h with respect to v varies from 0.33 for laminar flow to around 0.8 for turbulent flow [76].

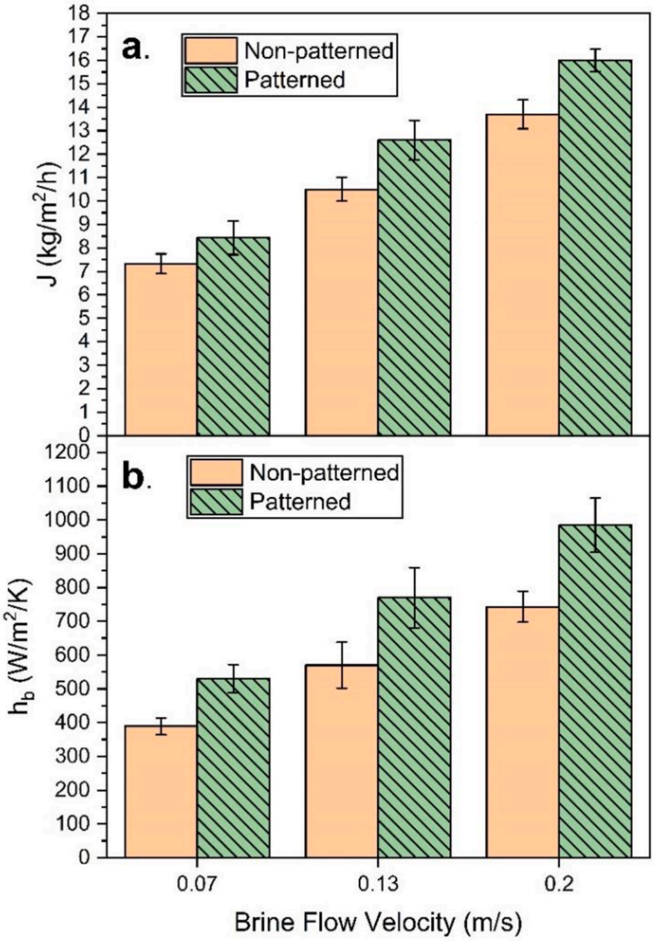

Fig. 6. (a) Water flux J and (b) brine-side heat transfer coefficient h_b for the non-patterned and patterned PVDF membranes as a function of brine flow velocity v_b. The DCMD process conditions: brine temperature = 60 °C, distillate temperature = 20 °C, NaCl concentration = 10 g/L.

The power law dependence in the small DCMD cell being around 0.6 indicates that the cell design in the small cell introduces a complicated flow regime. We expect that different surface patterns will introduce different '*n*' values, but these values are unlikely to differ by significant amounts. A way to determine the *n* value for a particular patterned surface is to develop a complementary CFD model. A significant difference may come if the primary feed flow direction is parallel to, perpendicular to, or at an angle to a particular surface pattern. The width of the gap between the contiguous ridges in each pattern is also likely to introduce an effect on '*n*' by affecting the local fluid flow pattern.

The DCMD performance of patterned and non-patterned membranes was compared in terms of the water flux (J) and h_b, as shown in Fig. 6. At constant brine and distillate temperatures, all membranes showed higher water flux with increased v_b, indicating better mixing in the boundary layer and higher thermal gradient across the MD membrane [77–79]. For example, J and h_b for the non-patterned membrane system increased by 87 % and 91 %, respectively, as v_b increased from 0.07 to 0.2 m/s (Fig. 6a and b).

At the same v_b, the presence of Sharklet patterns improved the water flux by about 15–17 % and h_b by 33–35 %, compared with non-patterned membranes. Evidently, the patterns improved the heat transfer, similar to the improved hydrodynamics within the boundary layer [39,40,52,54,61,80]. In comparison, feed spacers (hundreds of μm in geometry) can enhance h_b by up to 80 % because of the larger-scale disturbance to the bulk feed [34,35]. However, spacers (non-permeable) are not an inherent part of the membrane and can reduce the active surface area of the membranes. Furthermore, bulk flow disruption by spacers may exacerbate the pressure loss across the feed channel, which requires increasing pressurization of the feed. This will more likely lead to brine leakage during the MD processes.

Nevertheless, the water flux achieved in this study is lower than other commercial PVDF and polytetrafluoroethylene (PTFE) membranes, which are typically above 20 L/m^2 h under similar conditions [60]. The difference was attributed to the much larger thickness of the PVDF membranes fabricated in this work (210 μm) than commercial ones (~40–100 μm). Therefore, further reduction in the patterned membrane thickness is needed for potential large-scale applications [81].

$$\text{Thermal efficiency } (\varphi) = \frac{\text{Rate of collected water mass } \left(\frac{kg}{h}\right) \times \text{Latent heat of water } \left(\frac{kJ}{kg}\right)}{\text{Total heat transfer Rate } \left(\frac{kJ}{h}\right)} \times 100\% \qquad (15)$$

Table 1 summarizes the T_1 (estimated using equation (10)) at the surface of the membranes at all brine flow conditions. The Sharklet patterns improved the effective temperature by an average of 2 °C. The water vapor pressures on the brine side of DCMD for non-patterned and patterned membranes were calculated using the Antoine equation ($\log_{10} P(mmHg) = 8.017 - \frac{1730.6}{233.426+T_1}$) by neglecting the limited effect of salt on the water vaporization for the 1 wt% NaCl solution used. Sharklet patterns improved the water vapor pressure by ~10.5 %: from 1.19 to 1.52 psi for the non-patterned membranes to 1.32–1.66 psi for the patterned membranes (Table S1). Accordingly, the improved water vapor pressure for patterned membrane was estimated to increase water flux by an average of 12 % based on the DCMD mass transfer model that describes the transition region between Knudsen diffusion and molecular diffusion (calculations by Eqs. S1-S3 summarized in supporting information). Compared to the 15–17 % actual enhancement in water flux, the small discrepancy could be ascribed to the systematic errors associated with the model calculations and simplification. Similarly, a recent study demonstrated that a 1–2 °C increase in membrane surface temperature could lead to ~16 % higher water flux [36].

Table 1
Comparison of the effective brine-side membrane temperature T_1 and thermal efficiency between the non-patterned and patterned membranes at the steady state of DCMD.

Brine Flow Velocity	Effective Temperature (Non-patterned)	Effective Temperature (Patterned)	Thermal Efficiency (Non-patterned)	Thermal Efficiency (Patterned)
0.07 m/s	44.5 ± 1.2 °C	46.4 ± 1.4 °C	70.2 ± 3.5%	73.7 ± 2.8%
0.13 m/s	47.7 ± 1.1 °C	49.5 ± 1.6 °C	79.5 ± 3.7%	81.6 ± 4.4%
0.20 m/s	49.3 ± 1.4 °C	51.1 ± 0.9 °C	86.6 ± 6.6%	89.8 ± 4.1%

Lastly, the thermal efficiency (φ, as defined in Eq (15)) of the DCMD for all the systems was summarized in Table 1. The φ values of non-patterned and patterned membranes ranged from 70 % to 90 %. Due to the improved heat transfer discussed above, the φ increased by ~16 % as v_b increased from 0.07 to 0.2 m/s for both non-patterned and patterned membranes. In contrast, there was a marginal enhancement in φ of ~3 % by the Sharklet patterns at identical flow conditions, indicating that the effect of the Sharklet patterns on the thermal efficiency was less profound than that of a higher brine flow speed. Both the patterned and non-patterned membranes achieved above 80 % thermal efficiency at a high brine flow rate, similar to the predicted efficiency obtained using commercial PVDF and PTFE membranes as the thickness approached 200 μm [60]. Specifically, since the *lt*-TIPS membranes were twice as thick as the commercial membranes, the heat transfer during DCMD took place mainly through the convective flow of water vapor, thereby minimizing the heat lost due to conduction through the membrane [60,82]. Further enhancement in thermal efficiency is possible through geometric modifications of patterns to trigger a more substantial mixing effect in the boundary layer, similar to those reported for the membrane spacer system [49,83,84].

3.3. *Desalinate brine with DCMD*

The effectiveness of Sharklet patterns against salt-scaling was evaluated by comparing the performance of non-patterned and patterned membranes during DCMD treating the saturated $CaSO_4$ and hypersaline NaCl solutions. For all DCMD hypersaline brine tests, the temperatures of feed and distillate were kept at 60 °C and 20 °C, while the brine flow velocity of 0.2 m/s was used for the highest thermal efficiency of DCMD [44,60,85].

3.3.1. *Super-saturated $CaSO_4$ solution*

$CaSO_4$ is one of the main constituent salts in the brine concentrates from desalination plants [86]. The sparing solubility of $CaSO_4$ in water renders its high scaling propensity on the membrane surface when the salt concentration is beyond the saturation point (2.0 g/L) [62,87]. The $CaSO_4$ scaling on the membrane surface and into pores leads to either pore blockage or brine leakage [88,89]. Fig. 7a and b shows the DCMD of saturated $CaSO_4$ solution in terms of water flux and salt rejection as a function of concentration factor for the non-patterned and patterned membranes, respectively. The water flux and conductivity of the bulk permeate of the non-patterned and patterned membranes are shown in Figs. S11a and 11b, respectively. The water flux remained steady

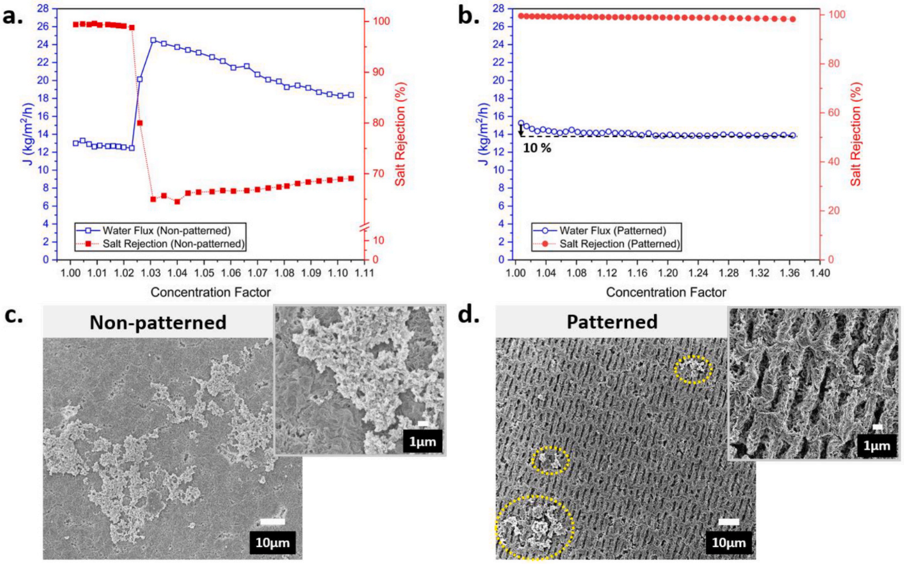

Fig. 7. Water flux and salt rejection comparison between the non-patterned (a) and patterned (b) membranes as a function of concentration factor throughout the DCMD of supersaturated $CaSO_4$ feed (initial $CaSO_4$ concentration of 2.0 g/L). Post-mortem SEM images of the $CaSO_4$ crystal depositions on the non-patterned (c) and patterned (d) membrane surface. The insets show the surface of both membranes at a higher magnification. The dashed circles in (d) indicate isolated $CaSO_4$ salt clusters on the patterned surface.

without observing large variation before reaching a concentration factor of 1.02 for the non-patterned membrane (Fig. 7a). Afterwards, a rapid increase of water flux by up to 96 % and a decrease of salt rejection from 98.8 to 65 % were detected at a concentration factor of 1.03 (the permeate conductivity increased from 1.4 to 58 μS/cm, Fig. S11a). These could be attributed to the diminished membrane surface hydrophobicity and the potential deformation of pores due to $CaSO_4$ scaling on the membrane surface and inside pores, which reduced the LEP of the

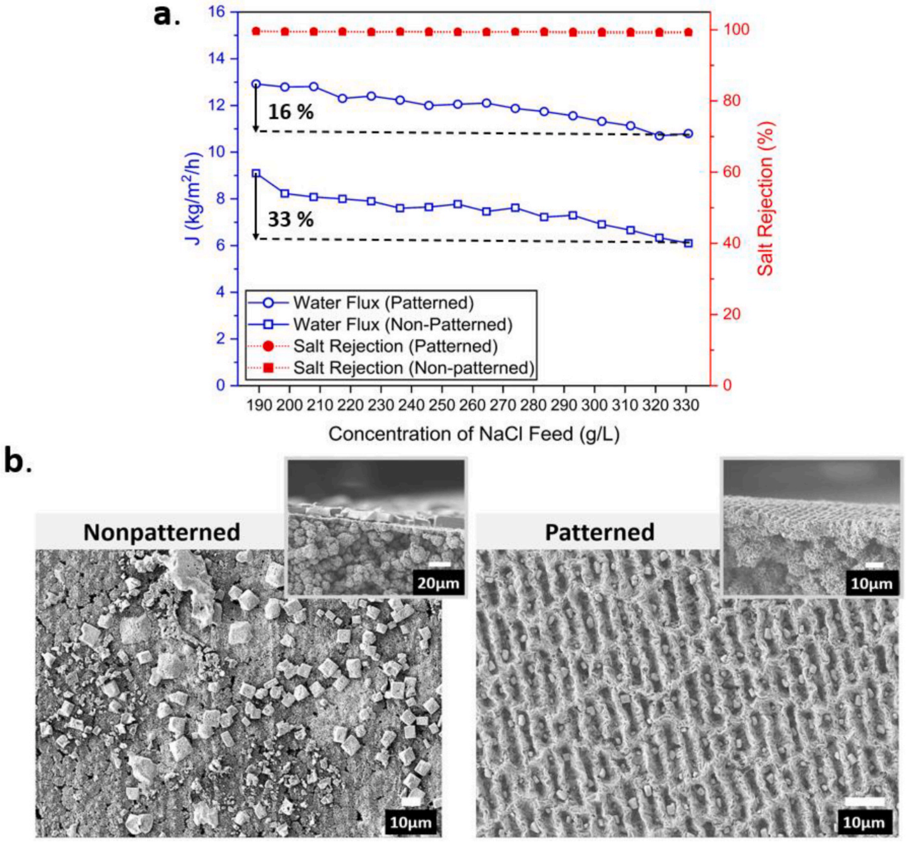

Fig. 8. (a) Comparison of water flux and salt rejection between the patterned and non-patterned membranes as a function of the real-time concentration of NaCl solution throughout the DCMD test. (b) Post-mortem SEM images of the salt deposition on the non-patterned (left) and patterned (right) membrane surfaces. The insets show the cross-sectional view of the scaling layers.

membrane [63]. The subsequent gradual reduction of water flux of non-patterned membranes from a concentration factor of 1.04 could be attributed to the blockage of pores. Specifically, the intruded salt crystals grew into large dimensions as DCMD proceeds, thus occupying the pore channels conformably. Nevertheless, the partial rejuvenation of salt rejection percentage (Fig. 7a) did not alleviate the salt leakage, given the conductivity of bulk permeate continued to increase from 58 to 132 μS/cm till the end of the test at a concentration factor around 1.1. In stark contrast, the initial water flux of the patterned membrane exceeded that of non-patterned counterpart by 15 %, which is in good agreement with the flux difference observed with the 1 wt% NaCl DCMD (Fig. 6a). Moreover, the patterned membrane exhibited a relatively steady water flux with an overall reduction of 10 % and >99 % salt rejection throughout the entire DCMD till concentration factor approaches 1.4 (Fig. 7b). The permeate conductivity was maintained below 20 μS/cm. The superior scaling resistance, benefiting from the enhanced surface shear stress of the patterned membrane, maintained a much cleaner surface without widely spread large crystal clusters (>20 μm) observed on non-patterned membrane (Fig. 7c), except for a few scatteringly distributed $CaSO_4$ crystal clusters (≤ 10 μm in dimension) as shown in Fig. 7d. Experiments were also done with a supersaturated solution of $CaSO_4$ at higher temperatures of 70 °C and 80 °C using earlier variety of non-patterned and patterned membranes which have higher thickness (∼450 μm). Table S2 summarizes the performance of those membranes in terms of flux enhancements as a result of the presence of Sharklet patterns. Similar to what was observed on the thinner PVDF membranes at lower temperatures, higher flux was achieved on all patterned membranes.

3.3.2. Hypersaline NaCl solution

The scaling resistance of the membranes was also investigated by performing DCMD of hypersaline NaCl solution with an initial salt concentration of 184 g/L, which was chosen to expedite the scaling. Fig. 8a shows the water flux and salt rejection of both the non-patterned and patterned membranes as a function of the real-time concentration of the NaCl solution. Note that the water flux of all *lt*-TIPS patterned membranes was comparable to that of the patterned PVDF membranes made by phase inversion micromolding [44]. The DCMD experiment was terminated at 72 h to protect the gear pump from corrosion. At the end of the 72 h test, the brine concentration reached 331 g/L.

Both patterned and non-patterned membranes did not show any significant brine leakage (salt rejection >99 %) throughout the tests (Fig. 8a). The final conductivity of bulk permeate was <200 μS/cm for all membranes (Fig. S12a). The patterned membrane showed 40 % higher water flux than the non-patterned membrane at the beginning of DCMD when scaling was insignificant, which was higher than that observed for the 1 wt% NaCl solution (17 %, Fig. 6a). The discrepancy was attributed to the alleviation of concentration polarization by the surface patterns [85], which was more significant for a more concentrated brine. Moreover, the patterned membrane showed a 16 % flux reduction, while the non-patterned membrane showed a 33 % reduction throughout the DCMD test. At the end of the test, the flux of the patterned membrane was up to 78 % higher than that of the non-patterned one.

From the post-mortem SEM analysis (Fig. 8b), cubic NaCl crystals with sizes up to 20 μm and a broad size distribution were observed randomly distributed across the non-patterned membrane surfaces. In certain regions (inset of Fig. 8b), a layer of crystals (thickness around 7 μm) covered the membrane surface. Similar clusters of salt crystals were also observed on other flat-surface membranes after the DCMD of NaCl feed [44,74]. In stark contrast, only smaller-sized (∼2 μm) crystals, with a uniform size distribution, were deposited within the grooves between pattern lines with no depositions on the pattern ridges. The difference in crystal deposition suggests that patterned membranes may retain a larger active surface area with fewer crystal depositions. From post-mortem WCA measurements, the salt deposition reduced the WCA from 1164 ± 1.6° to 91.8 ± 2.4° for the non-patterned membrane and from 137.5 ± 1.8° to 111.6 ± 2.6° for the patterned membrane (Fig. S13 a). The enhanced WCA of a clean patterned membrane can be described by the Cassie-Baxter equation

$$\cos \theta_a = f(1 + \cos \theta_0) - 1 \tag{16}$$

where f is the fraction of PVDF surface in contact with liquid, θ_a is the apparent WCA, and θ_0 is the intrinsic WCA of bulk PVDF, which is ∼85° for all non-chemically modified nonporous PVDF films [90]. The air entrapped within the trenches of the Sharklet patterns reduces the solid-liquid interface. Subsequently, the diminished f leads to a higher apparent WCA on the patterned membranes. Next, the PVDF membranes were challenged with an even more concentrated NaCl solution with a starting concentration of 314 g/L. The DCMD was continued till the brine solution reached the solubility limit of NaCl (∼370 g/L at 60 °C). Fig. 9a shows the water flux and salt rejection as a function of real-time NaCl concentration. Similar to the tests shown in Fig. 8, the patterned membrane was superior in terms of water flux over the non-patterned one. Specifically, the flux of the patterned membrane decreased by 24 % at the end of the test when the salt concentration approached the solubility limit of NaCl [91]. The flux of the non-patterned membrane was reduced by nearly 69 %, making the patterned membrane three times more permeable than the nonpatterned one. The salt rejection of the non-patterned membrane dropped below 99 % at a brine concentration of 361 g/L. In contrast, no salt leakage was observed on the patterned membrane until 3 h after the brine reached the solubility limit (the final conductivity of bulk permeate was ∼1400 μS/cm). This is interesting considering that both the non-patterned and patterned membranes were not chemically modified to acquire super-hydrophobicity against scaling and brine leakage, which were observed to occur almost instantaneously as the brine concentration approaches the solubility limit of salt [44,92].

Post-mortem SEM analysis showed that clusters of salt crystals covered the surface of both patterned and non-patterned membranes. Large salt crystals (∼100 μm) were observed on the non-patterned membrane with a characteristic cubic shape (Fig. 9b). In contrast, the crystal appeared "flake-like" on the patterned membrane surface, which suggests possible spatial confinement from the pattern lines that impact the growth salt crystals (inset of Fig. 9b). Accordingly, WCAs of the non-patterned and patterned membranes reduced to 72.6 ± 5.1° and 89.3 ± 2.3° (Fig. S8 b). Such a loss of hydrophobicity is consistent with the brine leakage observed during the DCMD process.

4. Conclusion

In this study, the *lt*-TIPS method is optimized to fabricate Sharklet-patterned PVDF membranes suitable for DCMD use. Using ATBC as the solvent for blade casting, Sharklet patterns are precisely imparted on the surface of PVDF membranes. The effect of casting speed and quenching medium on the patterning fidelity, pore size, porosity, and LEP are systematically examined. The optimized *lt*-TIPS process results in patterned membranes with the highest patterning fidelity of 80 %. The maximum pore size, overall porosity, and LEP are independent of the casting speed. The mean pore size appears to be impacted by the quenching medium, showing faster quenching in water leads to smaller open pores than quenching in air.

The impact of the Sharklet patterns on DCMD performance is systematically examined. The presence of Sharklet patterns, when aligned perpendicular to the brine flow, effectively improves the water flux by 15–17 % and the brine-side heat transfer coefficient by 33–35 %, which translates to an average of 3 % enhancement in thermal efficiency at brine flow velocities of 0.07–0.2 m/s. When treating hypersaline feeds with saturated $CaSO_4$ solution and hypersaline NaCl solutions with initial concentrations of 189 g/L and 314 g/L, the Sharklet patterns improve the initial water flux, alleviate flux decline, maintain a high salt

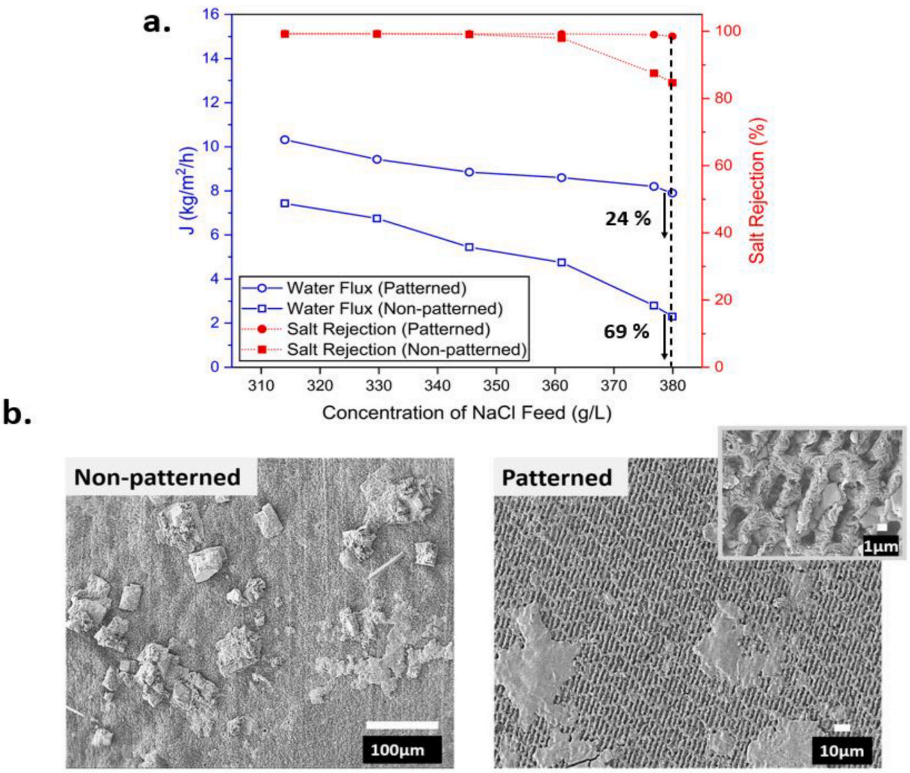

Fig. 9. (a) Comparison of water flux and salt rejection between the patterned and non-patterned PVDF membranes as a function of real-time concentration of NaCl. (b) Surface SEM images comparing the salt scaling on the non-patterned (left) and patterned (right) membrane surfaces (images in the upper right show the scaling on the patterned surface at higher magnification).

rejection, and delay brine leakage during DCMD. Post-mortem analysis reveals reduced salt crystal deposition on patterned membranes with smaller crystal sizes, indicating better retention of membrane hydrophobicity. These experimental findings demonstrate that Sharklet patterning of PVDF membranes through *lt*-TIPS provides an effective and simple approach to addressing the critical challenges for MD technologies in terms of temperature polarization, as well as scaling and brine leakage.

CRediT authorship contribution statement

Shouhong Fan: Writing – review & editing, Writing – original draft, Methodology, Investigation, Formal analysis, Data curation. **Duong T. Nguyen:** Data curation. **Jaylene Martinez:** Methodology, Data curation. **John Chau:** Methodology, Data curation. **Kieran Fung:** Methodology, Data curation. **Kamalesh Sirkar:** Writing – review & editing, Supervision, Resources, Project administration, Methodology, Investigation, Funding acquisition. **Anthony P. Straub:** Writing – review & editing, Resources, Methodology. **Yifu Ding:** Writing – review & editing, Supervision, Resources, Project administration, Methodology, Investigation, Funding acquisition, Formal analysis, Conceptualization.

Declaration of competing interest

The authors declare that they have no known competing financial interests or personal relationships that could have appeared to influence the work reported in this paper.

Acknowledgments

We acknowledge the support from the National Science Foundation (NSF) Industry/University Cooperative Research Center for Membrane Science, Engineering and Technology (MAST) at the University of Colorado Boulder (UCB, award number, IIP 1624602 & EEC 2310937). We also acknowledge funding support from Desalination and Water Purification Research (DWPR) Program of the US Bureau of Reclamation (Grant# 13761646).

Appendix A. Supplementary data

Supplementary data to this article can be found online at https://doi.org/10.1016/j.memsci.2024.123476.

Data availability

Data will be made available on request.

References

[1] C. He, Z. Liu, J. Wu, X. Pan, Z. Fang, J. Li, B.A. Bryan, Future global urban water scarcity and potential solutions, Nat. Commun. 12 (2021) 4667, https://doi.org/10.1038/s41467-021-25026-3.

[2] M.M. Mekonnen, A.Y. Hoekstra, Four billion people facing severe water scarcity, Sci. Adv. 2 (2016) e1500323, https://doi.org/10.1126/sciadv.1500323.

[3] M. Issaoui, S. Jellali, A.A. Zorpas, P. Dutournie, Membrane technology for sustainable water resources management: challenges and future projections, Sustainable Chemistry and Pharmacy 25 (2022) 100590, https://doi.org/10.1016/j.scp.2021.100590.

[4] E. Jones, M. Qadir, M.T.H. Van Vliet, V. Smakhtin, S. Kang, The state of desalination and brine production: a global outlook, Sci. Total Environ. 657 (2019) 1343–1356, https://doi.org/10.1016/j.scitotenv.2018.12.076.

[5] S. Adham, A. Hussain, J.M. Matar, R. Dores, A. Janson, Application of Membrane Distillation for desalting brines from thermal desalination plants, Desalination 314 (2013) 101–108, https://doi.org/10.1016/j.desal.2013.01.003.

[6] J. Swaminathan, H.W. Chung, D.M. Warsinger, J.H. Lienhard V, Energy efficiency of membrane distillation up to high salinity: evaluating critical system size and optimal membrane thickness, Appl. Energy 211 (2018) 715–734, https://doi.org/10.1016/j.apenergy.2017.11.043.

[7] T.Y. Cath, V.D. Adams, A.E. Childress, Experimental study of desalination using direct contact membrane distillation: a new approach to flux enhancement, J. Membr. Sci. 228 (2004) 5–16, https://doi.org/10.1016/j.memsci.2003.09.006.

[8] J. Li, Y. Guan, F. Cheng, Y. Liu, Treatment of high salinity brines by direct contact membrane distillation: effect of membrane characteristics and salinity, Chemosphere 140 (2015) 143–149, https://doi.org/10.1016/j.chemosphere.2014.12.006.

[9] H.C. Duong, A.R. Chivas, B. Nelemans, M. Duke, S. Gray, T.Y. Cath, L.D. Nghiem, Treatment of RO brine from CSG produced water by spiral-wound air gap membrane distillation — a pilot study, Desalination 366 (2015) 121–129, https://doi.org/10.1016/j.desal.2014.10.026.

[10] B.B. Ashoor, S. Mansour, A. Giwa, V. Dufour, S.W. Hasan, Principles and applications of direct contact membrane distillation (DCMD): a comprehensive review, Desalination 398 (2016) 222–246, https://doi.org/10.1016/j.desal.2016.07.043.

[11] J. Wang, Y. Liu, U. Rao, M. Dudley, N.D. Ebrahimi, J. Lou, F. Han, E.M.V. Hoek, N. Tilton, T.Y. Cath, C.S. Turchi, M.B. Heeley, Y.S. Ju, D. Jassby, Conducting thermal energy to the membrane/water interface for the enhanced desalination of hypersaline brines using membrane distillation, J. Membr. Sci. 626 (2021) 119188, https://doi.org/10.1016/j.memsci.2021.119188.

[12] P. Wang, T.-S. Chung, Recent advances in membrane distillation processes: membrane development, configuration design and application exploring, J. Membr. Sci. 474 (2015) 39–56, https://doi.org/10.1016/j.memsci.2014.09.016.

[13] J. Xu, Y.B. Singh, G.L. Amy, N. Ghaffour, Effect of operating parameters and membrane characteristics on air gap membrane distillation performance for the treatment of highly saline water, J. Membr. Sci. 512 (2016) 73–82, https://doi.org/10.1016/j.memsci.2016.04.010.

[14] T. Tong, M. Elimelech, The global rise of zero liquid discharge for wastewater management: drivers, technologies, and future directions, Environ. Sci. Technol. 50 (2016) 6846–6855, https://doi.org/10.1021/acs.est.6b01000.

[15] M. Rezaei, D.M. Warsinger, J.H. Lienhard V, M.C. Duke, T. Matsuura, W. M. Samhaber, Wetting phenomena in membrane distillation: mechanisms, reversal, and prevention, Water Res. 139 (2018) 329–352, https://doi.org/10.1016/j.watres.2018.03.058.

[16] V.R. Moreira, J.V. Raad, J.X. Lazarini, L.V.S. Santos, M.C.S. Amaral, Recent progress in membrane distillation configurations powered by renewable energy sources and waste heat, Journal of Water Process Engineering 53 (2023) 103816, https://doi.org/10.1016/j.jwpe.2023.103816.

[17] L.D. Nghiem, T. Cath, A scaling mitigation approach during direct contact membrane distillation, Separ. Purif. Technol. 80 (2011) 315–322, https://doi.org/10.1016/j.seppur.2011.05.013.

[18] A. Anvari, A. Azimi Yancheshme, K.M. Kekre, A. Ronen, State-of-the-art methods for overcoming temperature polarization in membrane distillation process: a review, J. Membr. Sci. 616 (2020) 118413, https://doi.org/10.1016/j.memsci.2020.118413.

[19] M. Rezaei, D.M. Warsinger, J.H. Lienhard V, W.M. Samhaber, Wetting prevention in membrane distillation through superhydrophobicity and recharging an air layer on the membrane surface, J. Membr. Sci. 530 (2017) 42–52, https://doi.org/10.1016/j.memsci.2017.02.013.

[20] D.M. Warsinger, J. Swaminathan, E. Guillen-Burrieza, H.A. Arafat, J.H. Lienhard V, Scaling and fouling in membrane distillation for desalination applications: a review, Desalination 356 (2015) 294–313, https://doi.org/10.1016/j.desal.2014.06.031.

[21] A. Alkhudhiri, N. Darwish, N. Hilal, Membrane distillation: a comprehensive review, Desalination 287 (2012) 2–18, https://doi.org/10.1016/j.desal.2011.08.027.

[22] S. Srisurichan, R. Jiraratananon, A. Fane, Mass transfer mechanisms and transport resistances in direct contact membrane distillation process, J. Membr. Sci. 277 (2006) 186–194, https://doi.org/10.1016/j.memsci.2005.10.028.

[23] P. Termpiyakul, R. Jiraratananon, S. Srisurichan, Heat and mass transfer characteristics of a direct contact membrane distillation process for desalination, Desalination 177 (2005) 133–141, https://doi.org/10.1016/j.desal.2004.11.019.

[24] A. Deshmukh, C. Boo, V. Karanikola, S. Lin, A.P. Straub, T. Tong, D.M. Warsinger, M. Elimelech, Membrane distillation at the water-energy nexus: limits, opportunities, and challenges, Energy Environ. Sci. 11 (2018) 1177–1196, https://doi.org/10.1039/C8EE00291F.

[25] A. Razmjou, E. Arifin, G. Dong, J. Mansouri, V. Chen, Superhydrophobic modification of TiO2 nanocomposite PVDF membranes for applications in membrane distillation, J. Membr. Sci. 415–416 (2012) 850–863, https://doi.org/10.1016/j.memsci.2012.06.004.

[26] Z. Ma, X. Chen, M. Jia, H. Mao, M. Li, S. Zhou, J.H. Xin, Y. Zhao, Superhydrophobic composite membranes for membrane distillation based on CNTs networks: overcoming the trade-off between water vapor permeability and wetting resistance, Separ. Purif. Technol. 341 (2024) 126861, https://doi.org/10.1016/j.seppur.2024.126861.

[27] Y. Liao, G. Zheng, J.J. Huang, M. Tian, R. Wang, Development of robust and superhydrophobic membranes to mitigate membrane scaling and fouling in membrane distillation, J. Membr. Sci. 601 (2020) 117962, https://doi.org/10.1016/j.memsci.2020.117962.

[28] C. Yang, M. Tian, Y. Xie, X.-M. Li, B. Zhao, T. He, J. Liu, Effective evaporation of CF4 plasma modified PVDF membranes in direct contact membrane distillation, J. Membr. Sci. 482 (2015) 25–32, https://doi.org/10.1016/j.memsci.2015.01.059.

[29] A. Anvari, K.M. Kekre, A. Azimi Yancheshme, Y. Yao, A. Ronen, Membrane distillation of high salinity water by induction heated thermally conducting membranes, J. Membr. Sci. 589 (2019) 117253, https://doi.org/10.1016/j.memsci.2019.117253.

[30] N. Sun, J. Li, J. Ren, Z. Xu, H. Sun, Z. Du, H. Zhao, R. Ettelatie, F. Cheng, Insights into the enhanced flux of graphene oxide composite membrane in direct contact membrane distillation: the different role at evaporation and condensation interfaces, Water Res. 212 (2022) 118091, https://doi.org/10.1016/j.watres.2022.118091.

[31] A. Politano, P. Argurio, G. Di Profio, V. Sanna, A. Cupolillo, S. Chakraborty, H. A. Arafat, E. Curcio, Photothermal membrane distillation for seawater desalination, Adv. Mater. 29 (2017) 1603504, https://doi.org/10.1002/adma.201603504.

[32] Q. Huang, S. Gao, Y. Huang, M. Zhang, C. Xiao, Study on photothermal PVDF/ATO nanofiber membrane and its membrane distillation performance, J. Membr. Sci. 582 (2019) 203–210, https://doi.org/10.1016/j.memsci.2019.04.019.

[33] B. Zhang, P.W. Wong, J. Guo, Y. Zhou, Y. Wang, J. Sun, M. Jiang, Z. Wang, A.K. An, Transforming Ti3C2Tx MXene's intrinsic hydrophilicity into superhydrophobicity for efficient photothermal membrane desalination, Nat. Commun. 13 (2022) 3315, https://doi.org/10.1038/s41467-022-31028-6.

[34] Y.-D. Kim, L. Francis, J.-G. Lee, M.-G. Ham, N. Ghaffour, Effect of non-woven net spacer on a direct contact membrane distillation performance: experimental and theoretical studies, J. Membr. Sci. 564 (2018) 193–203, https://doi.org/10.1016/j.memsci.2018.07.019.

[35] J. Seo, Y.M. Kim, J.H. Kim, Spacer optimization strategy for direct contact membrane distillation: shapes, configurations, diameters, and numbers of spacer filaments, Desalination 417 (2017) 9–18, https://doi.org/10.1016/j.desal.2017.05.009.

[36] S. Jeong, Y. Jeong, B. Gu, S. Jeong, Comparative study of anti-scaling performance in membrane distillation: membrane spacer vs. patterned module vs. patterned membrane, Chem. Eng. J. 493 (2024) 152470, https://doi.org/10.1016/j.cej.2024.152470.

[37] S.H. Maruf, L. Wang, A.R. Greenberg, J. Pellegrino, Y. Ding, Use of nanoimprinted surface patterns to mitigate colloidal deposition on ultrafiltration membranes, J. Membr. Sci. 428 (2013) 598–607, https://doi.org/10.1016/j.memsci.2012.10.059.

[38] S.H. Maruf, Z. Li, J.A. Yoshimura, J. Xiao, A.R. Greenberg, Y. Ding, Influence of nanoimprint lithography on membrane structure and performance, Polymer 69 (2015) 129–137, https://doi.org/10.1016/j.polymer.2015.05.049.

[39] S.H. Maruf, M. Rickman, L. Wang, J. Mersch Iv, A.R. Greenberg, J. Pellegrino, Y. Ding, Influence of sub-micron surface patterns on the deposition of model proteins during active filtration, J. Membr. Sci. 444 (2013) 420–428, https://doi.org/10.1016/j.memsci.2013.05.060.

[40] Y. Ding, S. Maruf, M. Aghajani, A.R. Greenberg, Surface patterning of polymeric membranes and its effect on antifouling characteristics, Separ. Sci. Technol. 52 (2017) 240–257, https://doi.org/10.1080/01496395.2016.1201115.

[41] C. Lee, G.W. Lee, W. Choi, C.H. Yoo, B. Chun, J.S. Lee, J.-H. Lee, H.W. Jung, Pattern flow dynamics over rectangular Sharklet patterned membrane surfaces, Appl. Surf. Sci. 514 (2020) 145961, https://doi.org/10.1016/j.apsusc.2020.145961.

[42] J.A. Kharraz, A.K. An, Patterned superhydrophobic polyvinylidene fluoride (PVDF) membranes for membrane distillation: enhanced flux with improved fouling and wetting resistance, J. Membr. Sci. 595 (2020) 117596, https://doi.org/10.1016/j.memsci.2019.117596.

[43] Y.K. Lee, Y.-J. Won, J.H. Yoo, K.H. Ahn, C.-H. Lee, Flow analysis and fouling on the patterned membrane surface, J. Membr. Sci. 427 (2013) 320–325, https://doi.org/10.1016/j.memsci.2012.10.010.

[44] Z. Xiao, R. Zheng, Y. Liu, H. He, X. Yuan, Y. Ji, D. Li, H. Yin, Y. Zhang, X.-M. Li, T. He, Slippery for scaling resistance in membrane distillation: a novel porous micropillared superhydrophobic surface, Water Res. 155 (2019) 152–161, https://doi.org/10.1016/j.watres.2019.01.036.

[45] J. Hu, H.B. Harandi, Y. Chen, L. Zhang, H. Yin, T. He, Anisotropic gypsum scaling of corrugated polyvinylidene fluoride hydrophobic membrane in direct contact membrane distillation, Water Res. 244 (2023) 120513, https://doi.org/10.1016/j.watres.2023.120513.

[46] X. Liao, S. Chou, C. Gu, X. Zhang, M. Shi, X. You, Y. Liao, A.G. Razaqpur, Engineering omniphobic corrugated membranes for scaling mitigation in membrane distillation, J. Membr. Sci. 665 (2023) 121130, https://doi.org/10.1016/j.memsci.2022.121130.

[47] J. Hu, Z. Wang, T. He, Enhancing the scaling resistance of corrugated polyvinylidene fluoride hydrophobic membrane in membrane distillation: impact of CF4 plasma modification, pulse flow, and negative pressure, Separ. Purif. Technol. 354 (2024) 128704, https://doi.org/10.1016/j.seppur.2024.128704.

[48] Y. Liu, T. Horseman, Z. Wang, H.A. Arafat, H. Yin, S. Lin, T. He, Negative pressure membrane distillation for excellent gypsum scaling resistance and flux enhancement, Environ. Sci. Technol. 56 (2022) 1405–1412, https://doi.org/10.1021/acs.est.1c07144.

[49] W. Choi, M.G. Shin, G.W. Lee, D. Kim, C.H. Yoo, J.S. Lee, H.W. Jung, J.-H. Lee, Anisotropic biofouling behavior of sharkskin-patterned desalination membranes, J. Membr. Sci. 683 (2023) 121814, https://doi.org/10.1016/j.memsci.2023.121814.

[50] S. Fan, M. Aghajani, M. Wang, J. Martinez, Y. Ding, Patterning flat-sheet Poly (vinylidene fluoride) membrane using templated thermally induced phase separation, J. Membr. Sci. 616 (2020) 118627, https://doi.org/10.1016/j.memsci.2020.118627.

[51] S. Fan, A. Blevins, J. Martinez, Y. Ding, Effects of Co-diluent on the pore structure, patterning fidelity, and properties of membranes fabricated by lithographically templated thermally induced phase separation, J. Membr. Sci. 662 (2022) 121023, https://doi.org/10.1016/j.memsci.2022.121023.

[52] O. Heinz, M. Aghajani, A.R. Greenberg, Y. Ding, Surface-patterning of polymeric membranes: fabrication and performance, Current Opinion in Chemical Engineering 20 (2018) 1–12, https://doi.org/10.1016/j.coche.2018.01.008.

[53] E. Drioli, A. Ali, F. Macedonio, Membrane distillation: recent developments and perspectives, Desalination 356 (2015) 56–84, https://doi.org/10.1016/j.desal.2014.10.028.

[54] W. Choi, C. Lee, D. Lee, Y.J. Won, G.W. Lee, M.G. Shin, B. Chun, T.-S. Kim, H.-D. Park, H.W. Jung, J.S. Lee, J.-H. Lee, Sharkskin-mimetic desalination membranes with ultralow biofouling, J. Mater. Chem. A 6 (2018) 23034–23045, https://doi.org/10.1039/C8TA06125D.

[55] J. Gutierrezrocca, J. Mcginity, Influence of water soluble and insoluble plasticizers on the physical and mechanical properties of acrylic resin copolymers, Int. J. Pharm. 103 (1994) 293–301, https://doi.org/10.1016/0378-5173(94)90180-5.

[56] Y.-J. Won, D.-C. Choi, J.H. Jang, J.-W. Lee, H.R. Chae, I. Kim, K.H. Ahn, C.-H. Lee, I.-C. Kim, Factors affecting pattern fidelity and performance of a patterned membrane, J. Membr. Sci. 462 (2014) 1–8, https://doi.org/10.1016/j.memsci.2014.03.012.

[57] H.H. Wang, J.T. Jung, J.F. Kim, S. Kim, E. Drioli, Y.M. Lee, A novel green solvent alternative for polymeric membrane preparation via nonsolvent-induced phase separation (NIPS), J. Membr. Sci. 574 (2019) 44–54, https://doi.org/10.1016/j.memsci.2018.12.051.

[58] A. Shrestha, J. Pellegrino, S.M. Husson, S.R. Wickramasinghe, A modified porometry approach towards characterization of MF membranes, J. Membr. Sci. 421–422 (2012) 145–153, https://doi.org/10.1016/j.memsci.2012.07.005.

[59] Y. Guan, J. Li, F. Cheng, J. Zhao, X. Wang, Influence of salt concentration on DCMD performance for treatment of highly concentrated NaCl, KCl, MgCl2 and MgSO4 solutions, Desalination 355 (2015) 110–117, https://doi.org/10.1016/j.desal.2014.10.005.

[60] L. Li, K.K. Sirkar, Influence of microporous membrane properties on the desalination performance in direct contact membrane distillation, J. Membr. Sci. 513 (2016) 280–293, https://doi.org/10.1016/j.memsci.2016.04.015.

[61] M. Xie, W. Luo, S.R. Gray, Surface pattern by nanoimprint for membrane fouling mitigation: design, performance and mechanisms, Water Res. 124 (2017) 238–243, https://doi.org/10.1016/j.watres.2017.07.057.

[62] T.A. Hoang, H.M. Ang, A.L. Rohl, Effects of temperature on the scaling of calcium sulphate in pipes, Powder Technol. 179 (2007) 31–37, https://doi.org/10.1016/j.powtec.2006.11.013.

[63] K.S.S. Christie, Y. Yin, S. Lin, T. Tong, Distinct behaviors between gypsum and silica scaling in membrane distillation, Environ. Sci. Technol. 54 (2020) 568–576, https://doi.org/10.1021/acs.est.9b06023.

[64] J.-H. Zuo, P. Cheng, X.-F. Chen, X. Yan, Y.-J. Guo, W.-Z. Lang, Ultrahigh flux of polydopamine-coated PVDF membranes quenched in air via thermally induced phase separation for oil/water emulsion separation, Separ. Purif. Technol. 192 (2018) 348–359, https://doi.org/10.1016/j.seppur.2017.10.027.

[65] T.-Q. Zhang, S. Hao, J. Xiao, Z.-Q. Jia, Preparation of poly(4-methyl-1-pentene) membranes by low-temperature thermally induced phase separation, ACS Appl. Polym. Mater. 5 (2023) 1998–2005, https://doi.org/10.1021/acsapm.2c02064.

[66] H. Matsuyama, H. Karkhanechi, S. Rajabzadeh, Polymeric membrane fabrication via thermally induced phase separation (TIPS) method, in: Hollow Fiber Membranes, Elsevier, 2021, pp. 57–83, https://doi.org/10.1016/B978-0-12-821876-1.00021-4.

[67] J.F. Kim, J.H. Kim, Y.M. Lee, E. Drioli, Thermally induced phase separation and electrospinning methods for emerging membrane applications: a review, AIChE J. 62 (2016) 461–490, https://doi.org/10.1002/aic.15076.

[68] B. Zhou, Y. Tang, Q. Li, Y. Lin, M. Yu, Y. Xiong, X. Wang, Preparation of polypropylene microfiltration membranes via thermally induced (solid–liquid or liquid–liquid) phase separation method, J. Appl. Polym. Sci. 132 (2015) 42490, https://doi.org/10.1002/app.42490.

[69] Z. Cui, N.T. Hassankiadeh, S.Y. Lee, J.M. Lee, K.T. Woo, A. Sanguineti, V. Arcella, Y.M. Lee, E. Drioli, Poly(vinylidene fluoride) membrane preparation with an environmental diluent via thermally induced phase separation, J. Membr. Sci. 444 (2013) 223–236, https://doi.org/10.1016/j.memsci.2013.05.031.

[70] J. Ravi, M.H.D. Othman, T. Matsuura, M. Ro'il Bilad, T.H. El-badawy, F. Aziz, A. F. Ismail, M.A. Rahman, J. Jaafar, Polymeric membranes for desalination using membrane distillation: a review, Desalination 490 (2020) 114530, https://doi.org/10.1016/j.desal.2020.114530.

[71] P. Yazgan-Birgi, M.I. Hassan Ali, H.A. Arafat, Estimation of liquid entry pressure in hydrophobic membranes using CFD tools, J. Membr. Sci. 552 (2018) 68–76, https://doi.org/10.1016/j.memsci.2018.01.061.

[72] E. Guillen-Burrieza, A. Servi, B.S. Lalia, H.A. Arafat, Membrane structure and surface morphology impact on the wetting of MD membranes, J. Membr. Sci. 483 (2015) 94–103, https://doi.org/10.1016/j.memsci.2015.02.024.

[73] K.J. Alvine, Y. Ding, J.F. Douglas, H.W. Ro, B.C. Okerberg, A. Karim, C.L. Soles, Capillary instability in nanoimprinted polymer films, Soft Matter 5 (2009) 2913, https://doi.org/10.1039/b901409h.

[74] J.A. Kharraz, M.R. Bilad, H.A. Arafat, Flux stabilization in membrane distillation desalination of seawater and brine using corrugated PVDF membranes, J. Membr. Sci. 495 (2015) 404–414, https://doi.org/10.1016/j.memsci.2015.08.039.

[75] N. Jamshidi, M. Farhadi, D.D. Ganji, K. Sedighi, Experimental analysis of heat transfer enhancement in shell and helical tube heat exchangers, Appl. Therm. Eng. 51 (2013) 644–652, https://doi.org/10.1016/j.applthermaleng.2012.10.008.

[76] R.Byron Bird, E. Warren, Edwin N. Stewart, Lightfoot, Transport Phenomena, second ed., 2006.

[77] Y.M. Manawi, M.A.M.M. Khraisheh, A.K. Fard, F. Benyahia, S. Adham, A predictive model for the assessment of the temperature polarization effect in direct contact membrane distillation desalination of high salinity feed, Desalination 341 (2014) 38–49, https://doi.org/10.1016/j.desal.2014.02.028.

[78] P. Termpiyakul, R. Jiraratananon, S. Srisurichan, Heat and mass transfer characteristics of a direct contact membrane distillation process for desalination, Desalination 177 (2005) 133–141, https://doi.org/10.1016/j.desal.2004.11.019.

[79] T.-C. Chen, C.-D. Ho, H.-M. Yeh, Theoretical modeling and experimental analysis of direct contact membrane distillation, J. Membr. Sci. 330 (2009) 279–287, https://doi.org/10.1016/j.memsci.2008.12.063.

[80] T.C.A. Ng, Z. Lyu, C. Wang, S. Guo, W. Poh, Q. Gu, L. Zhang, J. Wang, H.Y. Ng, Effect of surface-patterned topographies of ceramic membranes on the filtration of activated sludge and their interaction with different particle sizes, J. Membr. Sci. 645 (2022) 120125, https://doi.org/10.1016/j.memsci.2021.120125.

[81] L. Eykens, I. Hitsov, K. De Sitter, C. Dotremont, L. Pinoy, I. Nopens, B. Van Der Bruggen, Influence of membrane thickness and process conditions on direct contact membrane distillation at different salinities, J. Membr. Sci. 498 (2016) 353–364, https://doi.org/10.1016/j.memsci.2015.07.037.

[82] H.Y. Wu, R. Wang, R.W. Field, Direct contact membrane distillation: an experimental and analytical investigation of the effect of membrane thickness upon transmembrane flux, J. Membr. Sci. 470 (2014) 257–265, https://doi.org/10.1016/j.memsci.2014.06.002.

[83] W. Choi, C. Lee, C.H. Yoo, M.G. Shin, G.W. Lee, T.-S. Kim, H.W. Jung, J.S. Lee, J.-H. Lee, Structural tailoring of sharkskin-mimetic patterned reverse osmosis membranes for optimizing biofouling resistance, J. Membr. Sci. 595 (2020) 117602, https://doi.org/10.1016/j.memsci.2019.117602.

[84] S.H. Maruf, A.R. Greenberg, J. Pellegrino, Y. Ding, Critical flux of surface-patterned ultrafiltration membranes during cross-flow filtration of colloidal particles, J. Membr. Sci. 471 (2014) 65–71, https://doi.org/10.1016/j.memsci.2014.07.071.

[85] J. Kim, H. Kwon, S. Lee, S. Lee, S. Hong, Membrane distillation (MD) integrated with crystallization (MDC) for shale gas produced water (SGPW) treatment, Desalination 403 (2017) 172–178, https://doi.org/10.1016/j.desal.2016.07.045.

[86] L.F. Greenlee, D.F. Lawler, B.D. Freeman, B. Marrot, P. Moulin, Reverse osmosis desalination: water sources, technology, and today's challenges, Water Res. 43 (2009) 2317–2348, https://doi.org/10.1016/j.watres.2009.03.010.

[87] L.D. Nghiem, T. Cath, A scaling mitigation approach during direct contact membrane distillation, Separ. Purif. Technol. 80 (2011) 315–322, https://doi.org/10.1016/j.seppur.2011.05.013.

[88] M. Gryta, Calcium sulphate scaling in membrane distillation process, Chem. Pap. 63 (2009), https://doi.org/10.2478/s11696-008-0095-y.

[89] T. Tong, A.F. Wallace, S. Zhao, Z. Wang, Mineral scaling in membrane desalination: mechanisms, mitigation strategies, and feasibility of scaling-resistant membranes, J. Membr. Sci. 579 (2019) 52–69, https://doi.org/10.1016/j.memsci.2019.02.049.

[90] A. Kaynak, T. Mehmood, X. Dai, K. Magniez, A. Kouzani, Study of radio frequency plasma treatment of PVDF film using Ar, O2 and (Ar + O2) gases for improved polypyrrole adhesion, Materials 6 (2013) 3482–3493, https://doi.org/10.3390/ma6083482.

[91] H. Langer, H. Offermann, On the solubility of sodium chloride in water, J. Cryst. Growth 60 (1982) 389–392, https://doi.org/10.1016/0022-0248(82)90116-6.

[92] F. He, J. Gilron, K.K. Sirkar, High water recovery in direct contact membrane distillation using a series of cascades, Desalination 323 (2013) 48–54, https://doi.org/10.1016/j.desal.2012.08.006.